

The Structure of the Milky Way's Hot Gas Halo

Matthew J. Miller, Joel N. Bregman

Department of Astronomy, University of Michigan, Ann Arbor, MI 48104

mjmil@umich.edu, jbregman@umich.edu

ABSTRACT

The Milky Way's million degree gaseous halo contains a considerable amount of mass that, depending on its structural properties, can be a significant mass component. In order to analyze the structure of the Galactic halo, we use *XMM-Newton* Reflection Grating Spectrometer archival data and measure O VII $K\alpha$ absorption-line strengths toward 26 active galactic nuclei, LMC X-3, and two Galactic sources (4U 1820-30 and X1735-444). We assume a β -model as the underlying gas density profile and find best-fit parameters of $n_o = 0.46^{+0.74}_{-0.35} \text{ cm}^{-3}$, $r_c = 0.35^{+0.29}_{-0.27} \text{ kpc}$, and $\beta = 0.71^{+0.13}_{-0.14}$. These parameters result in halo masses ranging between $M(18 \text{ kpc}) = 7.5^{+22.0}_{-4.6} \times 10^8 M_\odot$ and $M(200 \text{ kpc}) = 3.8^{+6.0}_{-0.5} \times 10^{10} M_\odot$ assuming a gas metallicity of $Z = 0.3 Z_\odot$, which are consistent with current theoretical and observational work. The maximum baryon fraction from our halo model of $f_b = 0.07^{+0.03}_{-0.01}$ is significantly smaller than the universal value of $f_b = 0.171$, implying the mass contained in the Galactic halo accounts for 10% - 50% of the missing baryons in the Milky Way. We also discuss our model in the context of several Milky Way observables, including ram pressure stripping in dwarf spheroidal galaxies, the observed X-ray emission measure in the 0.5 - 2 keV band, the Milky Way's star formation rate, spatial and thermal properties of cooler gas ($\sim 10^5 \text{ K}$) and the observed *Fermi* bubbles toward the Galactic center. Although the metallicity of the halo gas is a large uncertainty in our analysis, we place a lower limit on the halo gas between the Sun and the Large Magellanic Cloud (LMC). We find that $Z \gtrsim 0.2 Z_\odot$ based on the pulsar dispersion measure toward the LMC.

1. Introduction

The detection of hot gas at zero redshift by *Chandra*, *XMM-Newton*, and *FUSE* implies there exists a reservoir of gas that potentially contains a significant amount of baryonic mass in the Milky Way. However, there have only been detections of this hot Galactic halo with little detailed analysis of its structural properties using multiple sightlines until this point. If the density profile of this halo was constrained, the mass could be calculated and compared to the other baryon mass components of the Milky Way in an attempt to account for some or all of the "missing baryons" in the local universe.

There has been extensive work in detecting and analyzing hot gaseous halos in galaxies other than the Milky Way as probes of galaxy formation and evolution. Detailed analyses of individual galaxies have revealed that other galaxies have considerable amounts of mass in their extended gaseous halos, but there is not enough to account for their missing baryons (Bregman & Houck 1997; Li et al. 2008; Anderson & Bregman 2010, 2011). In addition to detailed analyses of individual galaxies, there have been numerous studies of the global properties of diffuse X-ray emission around galaxies (O’Sullivan et al. 2003; Strickland et al. 2004; Tüllmann et al. 2006). These properties offer a foundation for comparing the Milky Way’s gaseous halo to other galaxies.

The primary tracers of the Milky Way’s hot gas halo are O VII and O VIII that exist in the 10^6 - 10^7 K range (Paerels & Kahn 2003). These X-ray lines have primarily been observed in absorption of active galactic nuclei (AGNs) and blazar spectra (Nicastrò et al. 2002; Rasmussen et al. 2003; Wang et al. 2005; Williams et al. 2005; Fang et al. 2006; Yao & Wang 2007; Hagihara et al. 2010) as well as Galactic X-ray binary spectra (Yao & Wang 2005; Hagihara et al. 2011) using *Chandra* and *XMM-Newton*. The lines have also been observed in emission with the Diffuse X-Ray Spectrometer by McCammon et al. (2002). In addition to this X-ray emitting/absorbing gas, O VI, the most common ion in $\sim 10^{5.5}$ K gas, has been extensively studied with *FUSE* (Sembach et al. 2003; Wakker et al. 2003; Fox et al. 2004). While the interaction between these gas phases is an area of interest, mass estimates from this cooler gas have not helped solve the missing baryon problem.

The structural properties of the Galactic halo have not been well constrained up until this point. The combination of O VII emission and absorption has constrained the temperature of the halo to be between $\log T = 6.1$ - 6.4 , however these estimates come primarily from analyses of single lines of sight toward the highest signal-to-noise (S/N) targets (Wang et al. 2005; Yao & Wang 2007; Hagihara et al. 2010). Attempts to constrain the density profile and thus the mass of the halo have been limited by the number of extragalactic lines of sight with high enough S/N (Bregman & Lloyd-Davies 2007; Gupta et al. 2012) or by only using Galactic sources to constrain the density profile (Yao & Wang 2005). If the halo extends past the disk of the galaxy, the density profile could only be constrained with multiple extragalactic sightlines.

Bregman & Lloyd-Davies (2007) studied O VII absorption lines using the Reflection Grating Spectrometer (RGS) on *XMM-Newton* with the goal to determine if these zero redshift absorption lines were from gas associated with the Milky Way’s halo or from a Local Group medium. This size discrepancy between these two scenarios is critical in terms of estimating the baryon mass of gas at this temperature. Their analysis indicated the equivalent widths of O VII lines are positively correlated with angle toward the Galactic center as opposed to M31 (toward the center of mass of the Local Group). This implies these lines originate in a gas reservoir confined to the Milky Way as opposed to the Local Group.

In this paper, we expand upon Bregman & Lloyd-Davies (2007) by adding three additional targets to our sample (one AGN and two Galactic targets) as well as provide a more detailed analysis of the structure and global properties of the hot Galactic halo, specifically the density

profile. We use O VII column densities along different sightlines throughout the Milky Way to determine the density profile of the hot Galactic halo. We then estimate the mass contained in the halo as well as compare our density profile with numerous observational constraints. The outline of the paper is as follows. In Section 2, we present our object selection and data analysis. In Section 3, we discuss our model fitting procedure as well as the different models we consider. In Section 4, we examine the consistency of our model with previously established constraints as well as compare our hot Galactic halo to different phases of the interstellar medium (ISM).

2. Object Selection

Our initial target list was identical to that of Bregman & Lloyd-Davies (2007), which was constructed from the brightest AGNs in the *XMM-Newton* RGS archival data. In addition to finding sources with suitable X-ray fluxes at 21.6 Å, the goal was also to find sources with O VII equivalent width uncertainties less than 10 mÅ (for typical equivalent widths of about 20 mÅ). This resulted in a sample of 25 AGNs plus an additional source in the Large Magellanic Cloud (LMC).

In addition to the original sample, we added an additional AGN (ESO 141-G055) and two Galactic low-mass X-ray binaries (LMXBs; 4U 1820-30, X1735-444) to our target list (Table 1). These added source spectra can be seen in Figure 1 while the distribution of our sources on the sky can be seen in Figure 2. The motivation for adding these sources is their proximity to the Galactic center. Two of the parameters of interest in our model fitting are sensitive to small galactocentric radii ($r \lesssim 2$ kpc), which would not be probed by the original sample (see Figure 2). The inclusion of these three sources allowed us to analyze the central region of the density profile better than the previous target list would have allowed. The additional targets also have small uncertainties in the measured equivalent widths ($\lesssim 25\%$) compared to the rest of the sample.

We are unable to distinguish between O VII halo gas absorption and intrinsic absorption for our Galactic targets due to the resolution of the RGS at 21.6 Å. However, the X-ray spectra of our two Galactic sources have been previously observed with no indication of intrinsic O VII absorption. There has been evidence for a photoionized wind from an accretion disk in 4U 1820-30 (Costantini et al. 2012). However this wind has only been detected in the lower ionization states of oxygen (O V and O VI) and not in the O VII absorption lines used in this study. Yao & Wang (2005) also analyzed X-ray spectra for a sample of Galactic sources, including X1735-444, to constrain the structure of the local hot ISM. They examine the possibility that some of the unresolved O VII absorption may come from photoionized winds, thus contaminating absorption from halo gas. However, they conclude this scenario is unlikely since the calculated radii where the lines would be produced are larger than the measured binary separations in six out of seven targets. We assume throughout our model fitting procedure that the O VII lines are entirely due to the halo gas and not associated with our LMXB targets.

The data reduction and data analysis for our sample was identical to that of Bregman & Lloyd-Davies (2007) since this work is an extension of their results. Thus, we refer the reader to the aforementioned paper for any details concerning the data acquisition, methods of fitting the spectra, or determining equivalent widths.

3. Model Fitting

Our model fitting procedure focuses on the comparison between measured electron column densities of our targets and theoretical column densities calculated by our model density profile. We consider both spherical and flattened density models in our model fitting procedure. The spherical profile is the simplest model we consider in the fitting process while the flattened profile adds one additional free parameter to account for the potential disk-like shape of the gas distribution. The coordinate transformations from a galactocentric density profile to a Sun-centered line of sight distance profile are

$$R^2 = R_o^2 + d^2 \cos(b)^2 - 2dR_o \cos(b) \cos(l) \tag{1}$$

$$z^2 = d^2 \sin(b)^2 \tag{2}$$

$$r^2 = R^2 + z^2 \tag{3}$$

In these coordinates, d is the line of sight distance, b and l are Galactic latitude and longitude, respectively, R_o is the distance from the Sun to the Galactic center (we assume 8.5 kpc throughout our analysis), and r is the galactocentric radius. We constrain the density profile of the halo by generating model column densities for a given set of model parameters and finding the parameter set that minimizes the χ^2 calculated from our data.

3.1. Column Density Calculation

In order to convert from measured O VII equivalent widths to total electron column densities, we follow several assumptions presented in Bregman & Lloyd-Davies (2007). We initially convert the equivalent widths to column densities assuming the lines are optically thin. In this case, the resulting linear conversion between the measured equivalent width and O VII column density is $N(\text{O VII}) = 3.48 \times 10^{14} \text{ EW}$, where EW is the O VII equivalent width in mÅ and the column density has units of cm^{-2} . However, recent work has shown the lines are likely mildly saturated based on the observed $K\beta$ to $K\alpha$ ratio for the O VII ion (Williams et al. 2005; Gupta et al. 2012). To analyze the saturation effects in our lines, we make assumptions on the Doppler widths of the lines since the lines are not resolved by the RGS. We expect the gas to be turbulent from supernovae mixing and subject to turbulent mixing layers between the hotter and cooler phases of halo gas (Begelman & Fabian 1990; Kwak & Shelton 2010). Thus, we assume the gas is turbulent at the

sound speed of hydrogen, which is consistent with simulations of halo gas (Fukugita & Peebles 2006; Cen 2012). This results in an assumed Doppler width of $b \approx 150 \text{ km s}^{-1}$. For a typical equivalent width in our sample ($\approx 20 \text{ m}\text{\AA}$) the optical depth at line center is of order unity, implying minor saturation corrections for our lines. To account for this, we initially calculate column densities linearly from our measured equivalent widths and determine correction factors using the curve of growth and assuming a Doppler width associated with turbulent motions discussed above. We use both sets of column densities to calculate best-fit parameters for our halo model due to the uncertainty in the Doppler widths of the lines and to examine how our best-fit parameters change after accounting for line saturation (see Section 4.4). However, we use the model fitting results from the saturated column densities in our analysis since the lines are expected to be minorly saturated. Both sets of column densities can be found in Table 1.

We make several assumptions while converting between O VII and total electron column densities. We assume that the abundance of oxygen is similar to the solar value and thus adopt a value of $\log(A_{\text{O}}) = 8.74$ (Holweger 2001). This results in a total electron column of

$$N_e = 4.4 \times 10^{19} \left(\frac{N_{\text{O VII}}}{10^{16} \text{ cm}^{-2}} \right) \left(\frac{f}{0.5} \right)^{-1} \left(\frac{Z}{Z_{\odot}} \right)^{-1} \text{ cm}^{-2} \quad (4)$$

where f is the ion fraction of O VII and Z is the metallicity of the gas. We assume an ion fraction of 0.5 for O VII, which is constrained by the temperature of the gas. We note that while we do assume a solar gas metallicity initially, the metallicity of the halo gas is a significant uncertainty in our analysis. We expect a portion of the halo to be enriched due to feedback from the Milky Way disk, but the true metallicity is likely less than the solar value. We discuss the implications of this assumption throughout our analysis.

3.2. Spherical Model

The simplest model we consider in our analysis is the β -model. We choose this model as opposed to a simpler model (such as a uniform density sphere) because it reproduces the observed X-ray surface brightness profiles of other galaxies (O’Sullivan et al. 2003). The β -model consists of three parameters and is defined as

$$n(r) = n_o(1 + (r/r_c)^2)^{-3\beta/2} \quad (5)$$

In this model, n_o is the core density, r_c is the core radius, and β is the slope of the profile at large radii. The parameters n_o and r_c describe the density near the center of the profile since n_o is the density at $r = 0$ and typical values for r_c are $\lesssim 1 \text{ kpc}$. These parameters are of little importance for mass estimates of the halo gas since majority of the mass comes from material at large radii.

On the other hand, β defines the behavior of the density profile at $r > r_c$ and is thus the primary parameter of interest.

Our best-fit parameters can be seen in Table 2 while the O VII column densities resulting from our best-fit models can be seen in Table 1. We also show how our observed saturated column densities compare with our best-fit model column densities in Figure 3. Initially, the best-fit model results in a χ^2 that is unacceptably large in both the optically thin and saturated column density conversions ($\chi^2_{thin}(\text{dof}) = 85.2$ (26), $\chi^2_{saturated}(\text{dof}) = 56.3$ (26)), which is possible if the variation due to substructure of the absorbing medium is larger than the statistical uncertainty of the equivalent widths. In order to account for this intrinsic variation, we add an additional uncertainty to all the equivalent widths of 7.5 mÅ for the optically thin column density conversion and 7.2 mÅ in the saturated case ($\sim 30\%$ of the average equivalent width). We also examine the variation in our calculated χ^2 to place a constraint on the halo size. Initially, we assume a halo size of 200 kpc when determining our best-fit parameters. By changing the size of the halo after we find our best-fit parameters, we can determine how the halo size changes the minimum χ^2 until our fit becomes unacceptable. We find a halo size 32 kpc at the 95% confidence level and 18 kpc at the 99% confidence level for both column density calculations.

The quality of the constraints on the halo parameters depends on both the quality of the data used as well as the location of our sources on the sky. The parameters n_o and r_c are the least constrained primarily due to only three of our targets passing near the Galactic center. In particular, the two Galactic targets that come closest to the Galactic center are less than 8.5 kpc away and thus do not probe the full inner region of the halo. Note that this would not be the case if r_c were larger, implying a more extended profile. The fact that these two parameters are not well constrained results from a degeneracy between them which is most apparent in Figure 4. To account for this, we note that for $r_c \ll r$ Equation (1) can be approximated by the power law

$$n(r) \approx \frac{n_o r_c^{3\beta}}{r^{3\beta}} \quad (6)$$

This reduces the dimensionality of the problem by making the free parameters a constant ($n_o r_c^{3\beta}$) and β . We expect the constraints on these parameters to be more reliable than the three parameter model due to the few lines of sight near the Galactic center. The 1σ , 2σ , and 3σ contours for all of our parameter spaces can be seen in Figure 4, considering the three and two parameter spherical models and using saturated column densities. We note little difference in the quality of our constraints between the three and two parameter spherical models. Fortunately, the parameter β is relatively well constrained for both models due to the majority of our sample being extragalactic targets.

3.3. Flattened Model

We also consider a flattened model in our fitting process by modifying the spherical β -model. The motivation behind considering a flattened density profile is based on the angular momentum associated with the Milky Way. The rotation of dark matter and baryons in the Milky Way could potentially alter a spherical gas profile into a flattened profile. We modify the traditional β -model in the following way:

$$n(r) = n_o(1 + (R/R_c)^2 + (z/z_c)^2)^{-3\beta/2} \quad (7)$$

In this flattened model, R is the radius in the plane of the disk and z is the height off of the Galactic plane with R_c and z_c representing the effective core radii for each coordinate. The parameters R_c and z_c are thus measures of density profile flattening. For this portion of our model fitting procedure, we fix the central density and slope of the density profile to their best-fit values associated with the spherical model and saturated column densities. Thus, we consider a flattened model only to see how the core radii associated with the orthogonal coordinates R and z change from a single, spherical core radius.

The best-fit parameters for our flattened model can be seen in Table 2. The flattened model initially has the same issue as the spherical model in that the best-fit parameters result in a χ^2 that is unacceptably large. Thus, we adopt the same procedure applied to the spherical model and add an additional uncertainty to the equivalent widths along each line of sight. We find that we must add the same additional uncertainty as the spherical case, $7.2 \text{ m}\text{\AA}$, to the equivalent widths to obtain an acceptable χ^2 . After accounting for this additional uncertainty, the best-fit parameters still result in core radii of less than 1 kpc and an axial ratio of $\sim 3/2$. The 1σ , 2σ , and 3σ contours for the core radii parameters can be seen in Figure 5 and indicate that profile is preferentially elongated in the R direction. However, the χ^2 change is small between the spherical and flattened models. This implies that the flattened and spherical models are equivalent in describing the density profile of the halo. Thus, we assume the density profile is spherical for the rest of our analysis for simplicity.

3.4. Negative Column Densities

Our sample contains three negative equivalent width measurements with corresponding negative column density conversions (see Table 1), which are possible if the S/N (the ratio between the measured equivalent width and corresponding uncertainty) is not sufficiently high for the observations. Although negative columns are not physical, we emphasize our measurements are all consistent with positive values based on their 1σ uncertainties and our model fitting procedure is sensitive to the difference between the measured and model column densities and the uncertainties associated with our measurements. Furthermore, the negative equivalent width measurements are not heavily weighted in our model fitting procedure due to their large uncertainties. We explore the effects of negative equivalent width measurements on our model fitting procedure by truncating

the negative measurements at zero and refitting the data assuming the same spherical model and saturation effects discussed above. The best-fit parameters for our sample with these truncated values are nearly identical to our results from our original sample. Alternatively, we apply a S/N cut to our sample to remove the negative equivalent width measurements from our model fitting procedure and determine how our results change. We choose a S/N threshold of 1.1, which removes the three negative equivalent width measurements as well as three positive measurements. The model fitting results from these two altered samples can be seen in Table 2. The best-fit parameters from these samples are consistent with our initial model fitting results based on their 1σ uncertainties. In particular, the parameter β is nearly identical between our initial and truncated sample results and shows a 16% variation between the initial and S/N cut sample results. It should be noted that both of these alterations to our sample impose a slight bias to our results toward the higher S/N observations, which may be due to strong absorption features or simply low noise measurements. However, our model fitting results are not strongly dependent to these changes due to the weak weighting of the low S/N measurements in our initial model fitting procedure. We therefore use the negative equivalent width measurements with uncertainties in our analysis, as opposed to truncating the values to zero or limiting our sample based on S/N, to retain the most information from the data.

We examine the validity of this model fitting approach by running Monte Carlo simulations to determine if we could recover our best-fit model parameters with the inclusion of negative column densities in our sample. For each line of sight, we assume the column density is normally distributed around its best-fit model value with σ defined by the measured uncertainty. Assuming these underlying normal distributions, we deviate the column densities from their best-fit model values and find new best-fit parameters for the deviated data. Figure 6 shows histograms of best-fit parameters β and $n_{or}r_c^{3\beta}$ from Equation (6) and the number of negative column densities in each simulation for 20,000 Monte Carlo simulations. Due to the large uncertainties for several of our column density measurements, our simulations consistently deviate column densities to negative values (median value of 7). The median values of β and $n_{or}r_c^{3\beta}$ are 0.71 and $0.050 \text{ cm}^{-3} \text{ kpc}^{3\beta}$, which are both consistent with our input values of 0.71 and $0.048 \text{ cm}^{-3} \text{ kpc}^{3\beta}$ for β and $n_{or}r_c^{3\beta}$, respectively. Furthermore, the distributions of β and $n_{or}r_c^{3\beta}$ are consistent with the 1σ boundaries of their best-fit values (see Table 2). This implies we reproduce our model fitting results with negative column densities in our sample and thus motivates the inclusion of the negative column density measurements in our sample.

4. Summary and Discussion

4.1. Spatial Distribution of the Gas

There has been recent work on the structure of the Milky Way’s hot gas halo utilizing the combination of emission ($\approx n_e^2 L$) and absorption ($\approx n_e L$) to constrain the density and size of the

halo gas. While our model is more sophisticated than a uniform density halo, these results serve as a foundation for comparing our density profile results. Bregman & Lloyd-Davies (2007) initially used the same *XMM – Newton* dataset as this paper without targets 27-29 (see Table 1) and found $n_e = 9 \times 10^{-4} \text{ cm}^{-3}$, $L = 19 \text{ kpc}$. Alternatively, Gupta et al. (2012) conducted a similar analysis with eight *Chandra* targets and found $n_e = 2 \times 10^{-4} \text{ cm}^{-3}$, $L = 72 \text{ kpc}$. Both of these results are more simplistic than our β -model and do not extend to the virial radius of the Milky Way. For comparison, we calculate the χ^2 for these models with our expanded dataset, while also including an additional uncertainty of 7.2 m\AA , and find $\chi^2(\text{dof}) = 39.5 (27)$ and $44.7 (27)$. Both of these are larger than the χ^2 we find for our best-fit model, $\chi^2 = 26.0 (26)$. Although the halo size is not a parameter in our model, our best-fit model is a statistical improvement over the uniform density models that have previously characterized the halo gas.

The best-fit parameters for our density model are also comparable to observations of hot gas halos around other galaxies where structural analysis has been possible. When comparing the Milky Way’s hot halo to that of other galaxies, the core radius and β parameters are the most applicable. The core density acts as a normalization of the overall profile and is physically not as significant as the other two parameters. O’Sullivan et al. (2003) conducted a study of early-type galaxies and extrapolated hot gas density profiles from the observed X-ray surface brightness profiles. Their model fitting procedure resulted in β values between 0.4 - 0.8 and core radii of less than 1 kpc for majority of their sample, both consistent with our best-fit parameters. There has also been more detailed work on the individual early-type galaxy NGC 1600. Sivakoff et al. (2004) analyzed the diffuse gas around NGC 1600 and found a two-component model to fit the surface brightness profile with $r_{c,in} = 4.2 \text{ kpc}$, $\beta_{in} = 1.18$, $r_{c,out} = 7.3 \text{ kpc}$, $\beta_{out} = 0.36$. The fitting results of NGC 1600 are odd in that a double β profile is not typically required to fit the X-ray surface brightness profiles around galaxies, particularly with β values that are inconsistent with analyses of other galaxies. This may be attributed to NGC 1600 residing in a group environment rather than in isolation. Detailed structure analysis of hot gas halos around late-type galaxies has been limited to only the most massive spirals. Anderson & Bregman (2011) analyzed the hot gas halo around NGC 1961 ($M_{vir} = 2.1 \times 10^{13} M_\odot$) and found $\beta = 0.47$ and $r_c = 1.00 \text{ kpc}$. Similarly, Dai et al. (2012) have analyzed the hot gas halo of UGC 12591 ($M_{vir} = 3.5 \times 10^{13} M_\odot$) and found $\beta = 0.48$ and $r_c = 3.04 \text{ kpc}$. Our measured β of 0.71 is steeper than observations of these massive spirals and the measured core radii for the most massive spirals are larger than the core radius determined for the Milky Way. The discrepancy between these parameters may be explained by the larger stellar disks and dark matter halos associated with NGC 1961 and UGC 12591 compared to the Milky Way. The comparison between the core radii and β parameters is also limited due to the weak constraint we have on the Milky Way’s core radius and the degeneracy between the core radius and core density.

The best-fit parameters from our model fitting procedure result in a density profile that is consistent with previously established constraints. The density model with best-fit parameters can be seen in Figure 7. Based on analyzing the pulsar dispersion measure toward the LMC, the average electron density between the Sun and the LMC must be $\langle n_e \rangle \leq 5 \times 10^{-4} \text{ cm}^{-3}$

(Anderson & Bregman 2010). For our density profile, the best-fit parameters result in an average electron density of $\langle n_e \rangle = 1.2 \times 10^{-4} \text{ cm}^{-3}$ between the Sun and the LMC assuming a solar metallicity. This is well below the upper limit established by the pulsar dispersion measure. The combination of having an upper limit to the average electron density between the Sun and the LMC and the fact that the total electron column density scales with metallicity as $\propto Z^{-1}$ (Equation (1)) allows us to place a lower limit on the metallicity of the gas toward the LMC. We find a minimum metallicity of $Z \gtrsim 0.2 Z_\odot$ in order to satisfy the pulsar dispersion measure toward the LMC. This lower limit is consistent with the metallicities of some high-velocity clouds (HVCs), particularly Complex C, and the Magellanic Stream (Gibson et al. 2000; van Woerden & Wakker 2004; Fox et al. 2005), implying the halo gas metallicity may be predominantly sub-solar.

We also examine the possibility of this hot gas extending out to the Milky Way’s virial radius, which would affect satellites of the Milky Way. There have been numerous studies investigating ram-pressure stripping of dwarf spheroidal galaxies orbiting the Milky Way, which implies the presence of a hot corona associated with the Milky Way out to ~ 200 kpc (Blitz & Robishaw 2000; Grcevich & Putman 2009). Blitz & Robishaw (2000) found that dwarf spheroidal galaxies orbiting the Milky Way will effectively lose their cold gas due to ram-pressure stripping for an ambient halo with density of $n \geq 2.4 \times 10^{-5} \text{ cm}^{-3}$ out to the virial radius of the Milky Way. Grcevich & Putman (2009) found a considerably larger value, $2.5 \times 10^{-4} \text{ cm}^{-3}$, out to similar distances. Our best-fit model results in densities that are too low to satisfy either of these constraints. In order to account for this we add an ambient density to our model of $n = 1 \times 10^{-5} \text{ cm}^{-3}$ out to 200 kpc. We choose a medium consistent with Blitz & Robishaw (2000) as opposed to Grcevich & Putman (2009) because an additional ambient medium as large as $2.5 \times 10^{-4} \text{ cm}^{-3}$ violates the observational constraint of the emission measure out of the Galactic plane, which will be discussed in greater detail in Section 4.2. We note that the addition of this density component does not change the best-fit parameters derived in our model fitting because the low ambient density does not contribute a significant fraction to the observed column densities. Thus, we can add this ambient medium to our density profile without jeopardizing the validity of our best-fit parameters.

We compare the scale height of our density model to the scale heights of different ions that represent different temperature phases of the ISM. The scale height is defined as

$$h = \left| \frac{n}{dn/dz} \right| = \frac{r_c^2}{3\beta z} \left(1 + \frac{R^2 + z^2}{r_c^2} \right) \quad (8)$$

When evaluating the scale height for our density model, we note that the function for the scale height is dependent on both R and z for our spherical model. We calculate the scale height for our profile at several different R and z distances (Table 3). The applicable comparison is for $R = 8.5$ kpc values since previous studies of other ions are inherently observed at the solar circle. The Li-like ions with peak abundances at temperatures 3, 2 and 1×10^5 K are O VI, N V and C IV (Sutherland & Dopita 1993). The scale heights of these ions have been measured to be $h(\text{O VI}, b > 0) = 4.6$, $h(\text{O VI}, b < 0) = 3.2$, $h(\text{N V}) = 3.9$, and $h(\text{C IV}) = 4.4$ kpc (Savage et al. 1997; Bowen et al.

2008). The scale height(s) we determine for O VII gas at $T \sim 10^6$ K are larger than these cooler ions by about an order of magnitude. This is expected due to the difference in temperature between the ions being approximately an order of magnitude. Thus, the distribution of our density model is more extended than the 10^5 K gas, indicating they are not cospatial (Williams et al. 2005).

4.2. Density and Mass Considerations

The primary goal for determining the density profile of the Milky Way’s hot gas halo is to determine the amount of mass it contains. The best-fit parameters and size of the halo determine whether there is enough mass contained in this temperature gas to account for some or all of the missing baryons in the Milky Way. The mass profile corresponding to the best-fit density profile can be seen in Figure 8 assuming the gas has a solar metallicity. We consider the mass contained within 18 kpc and 200 kpc as limits on the minimum and maximum mass of the halo. The minimum halo size is based on statistical arguments presented in Section 3.2 while we assume the halo extends to the Milky Way’s virial radius for a maximum halo size. Given our best-fit parameters, we find $M(18 \text{ kpc}) = 2.2^{+6.7}_{-1.3} \times 10^8 M_\odot$ and $M(200 \text{ kpc}) = 1.2^{+1.7}_{-0.2} \times 10^{10} M_\odot$. The mass contribution from the additional ambient medium discussed in Section 4.1 is substantial at 200 kpc ($\approx 7 \times 10^9 M_\odot$), but generally consistent with the error bars on our mass estimates. The known baryonic mass in the Milky Way (stars + cold gas) is approximately $5 \times 10^{10} M_\odot$ (Binney & Tremaine 2008). This implies stellar + cold gas to hot gas mass fractions of 230 (18 kpc) and 4 (200 kpc). We then compare the hot gas mass to the virial mass of the Milky Way ($\sim 2 \times 10^{12} M_\odot$) and define the baryon fraction as $f_b = M_b/M_{tot}$. The resulting baryon fractions are $f_b(18 \text{ kpc}) = 0.02^{+0.01}_{-0.01}$ and $f_b(200 \text{ kpc}) = 0.03^{+0.01}_{-0.01}$, both of which are much smaller than the value obtained from the *Wilkinson Microwave Anisotropy Probe* five-year data $f_b = 0.171 \pm 0.006$ (Dunkley et al. 2009).

There are several uncertainties in our analysis that can significantly change our mass estimate and corresponding baryon fraction. The virial mass of the Milky Way has been estimated to be between $1.0 - 2.4 \times 10^{12} M_\odot$ (Boylan-Kolchin et al. 2013). If we consider the virial mass of the Milky Way to be $1 \times 10^{12} M_\odot$ as opposed to $2 \times 10^{12} M_\odot$, the missing baryon mass is $1.5 \times 10^{11} M_\odot$ as opposed to $3.6 \times 10^{11} M_\odot$. This also changes the virial radius of the Milky Way by about a factor of ~ 0.8 ($r_{vir} \propto M_{vir}^{1/3}$). For a virial mass of $1 \times 10^{12} M_\odot$ and virial radius of 160 kpc, our best-fit model halo results in a hot gas mass and baryon fraction of $M(160 \text{ kpc}) = 6.5^{+13.2}_{-1.3} \times 10^9 M_\odot$ and $f_b(160 \text{ kpc}) = 0.05^{+0.02}_{-0.00}$. In this case, the halo gas bound to the Milky Way accounts for 5% - 15% of the missing baryons.

One possibility that increases the baryon fraction is halo gas extending beyond the Milky Way’s virial radius, implying the gas is not bound to the Milky Way. Given our best-fit parameters and the range of virial masses discussed above, the halo would need to be between 400 - 600 kpc ($\sim 3r_{vir}$) to account for the missing baryons. We are unable to rule out a halo this large since our results are insensitive to the low density gas that potentially exists at this radius. Other studies have explored the possibility of non-local O VII absorption by examining galaxies who have impact parameters

within 2-3 virial radii of a given AGN line of sight (Fang et al. 2006; Anderson & Bregman 2010). These nondetections of halo gas result in upper limits on the column densities of halo gas beyond the virial radii of other galaxies.

The metallicity of the halo gas also can potentially increase our mass estimates. We initially assumed a solar gas metallicity in our conversion from O VII to electron column density. However, we note $N_e \propto Z^{-1}$ (see Equation (4)), implying all of our inferred electron columns will increase if the metallicity is sub-solar. This effectively changes the normalization of our profile and results in $M \propto Z^{-1}$ for a given halo size. If we consider a halo gas metallicity of $Z = 0.3 Z_\odot$ (within the lower limit established by the pulsar dispersion measure toward the LMC), $M_{vir} = 1 \times 10^{12} M_\odot$ and a halo extending to the virial radius, our mass estimate and baryon fraction become $M(160 \text{ kpc}) = 2.2^{+4.4}_{-0.5} \times 10^{10} M_\odot$ and $f_b(160 \text{ kpc}) = 0.07^{+0.03}_{-0.01}$. The upper 1σ limit on this mass estimate adds a considerable amount of mass to the Milky Way, but only accounts for $\sim 50\%$ of the missing baryons.

Our mass estimates are comparable to observations of the Milky Way’s hot gas halo and simulations of the circumgalactic medium (CGM) around galaxies similar to the Milky Way. Although previous observations of the Milky Way’s hot gas halo have relied upon uniform density approximations (see Section 4.1), the derived masses are consistent with our model parameters with assumptions regarding the gas metallicity. The model found by Bregman & Lloyd-Davies (2007) resulted in a halo gas mass of $4 \times 10^8 M_\odot$ for a halo size of 20 kpc, which is consistent with our 1σ uncertainties for the enclosed mass at that radius. Alternatively, Gupta et al. (2012) found a lower limit on the halo gas mass of $> 6.1 \times 10^{10} M_\odot$ for $L > 139$ kpc assuming the gas metallicity is $0.3 Z_\odot$. Our halo model predicts a mass between $1.2 - 5.2 \times 10^{10} M_\odot$ for that same radius and metallicity. Our mass estimates are also in agreement with simulations of the CGM around Milky Way-sized galaxies if we assume a gas metallicity of $\sim 0.3 Z_\odot$. Hydrodynamical simulations by Feldmann et al. (2013) predict CGM densities of $\sim 10^{-4} \text{ cm}^{-3}$ out to ~ 100 kpc, resulting in mass estimates of $[0.2, 1.0, 3.5] \times 10^{10} M_\odot$ at $r = [50, 100, 200]$ kpc. These estimates are within our 1σ uncertainties at each radius for a gas metallicity of $\sim 0.3 Z_\odot$, indicating the halo gas mass is likely comparable to the observed stellar + cold gas mass previously observed for the Milky Way.

The enclosed hot gas mass near the disk of the Milky Way is comparable to the observed mass in ionized HVCs. The total mass of ionized HVCs within 5-15 kpc of the Sun is $M \approx 1.1 \times 10^8 (d/12 \text{ kpc})^2 (f_c/0.5) (Z/0.2Z_\odot)^{-1} M_\odot$, where f_c is the covering fraction (Lehner et al. 2012). For typical ionized HVC parameters, this mass estimate is approximately equal to the suggested hot gas mass enclosed within 10 kpc of the Galactic center (see Figure 8). One possibility to explain the similarity between these masses is that the ionized HVCs could have cooled out of the hot halo and are accreting on the disk of the Milky Way. However, the origin of HVCs is still poorly understood and likely a combination of several sources. The consistency between the mass estimates offers one possible formation mechanism.

The Milky Way’s hot gas halo has been observed in X-ray emission by several groups and

our density profile must be consistent with these observational constraints. We note that because the density profile of the gas falls off faster than $n \propto r^{-1}$ the column density is dominated by gas closest to the Galactic center. This effect is more drastic when we examine the X-ray emission of the halo due to the emission measure scaling as n^2 . We define the emission measure as

$$EM = \int_0^d n_e n_p ds \quad (9)$$

where we note that to be consistent with Equations (1)-(3), d is the line of sight distance and n_e and n_p are functions of both b and l .

One constraint we must address is the X-ray emission measure toward the Galactic center determined by Snowden et al. (1997) using the *ROSAT* all-sky survey. The observed count rate toward the Galactic center is $\sim 150 \times 10^{-6}$ counts s^{-1} arcmin^{-2} , which includes extinction in the Galactic plane. However, by assuming an absorbing column of 4.4×10^{21} H I cm^{-2} , they extrapolate a peak count rate of $\sim 900 \times 10^{-6}$ counts s^{-1} arcmin^{-2} for the 3/4 keV band. Using their conversion between count rate and emission measure, which is sensitive to temperature, we determine that the extrapolated count rate corresponds to an emission measure of 0.45 cm^{-6} pc. In order to reproduce this emission measure, we need to consider an inner radius where the density is constant for $0 \leq r \leq r_{in}$. We find that our density model must be constant at $n_{in} = 8.8 \times 10^{-3} \text{ cm}^{-3}$ out to an inner radius of $r_{in} = 2.2$ kpc to reproduce the observed emission measure toward the Galactic center. We note that this inner radius does not affect the other parts of our analysis. In particular, the mass estimate is not affected by this due to the small volume associated with this region. Also, we note that this inner radius is larger than the core radius of our profile. This is not a major concern since r_c is not well constrained and we still constrain the extended regions of the profile reasonably well.

The other emission measure constraint of interest is the emission measure out of the Galactic plane. McCammon et al. (2002) analyzed a 1 sr region of sky at $l = 90^\circ$, $b = +60^\circ$ using a quantum calorimeter sounding rocket. Their sensitivity and spectral resolution allowed them to model the soft X-ray diffuse background into an absorbed thermal component with $EM = 0.0037 \text{ cm}^{-6}$ pc and an unabsorbed thermal component with $EM = 0.0088 \text{ cm}^{-6}$ pc. Given our best-fit halo model, the predicted absorbed emission measure is $0.0017 (Z/Z_\odot) \text{ cm}^{-6}$ pc for $r_{halo} = 18$ kpc and $0.0018 (Z/Z_\odot) \text{ cm}^{-6}$ pc for $r_{halo} = 200$ kpc. This implies that the emission is dominated by the gas within ≈ 20 kpc of the Galactic center. The emission measure produced by our best-fit halo model underproduces the observed emission measure near $l = 90^\circ$, $b = +60^\circ$ regardless of the halo size we consider and for solar metallicity. However, the 1σ upper limit on our emission measure along this line of sight is $0.0122 (Z/Z_\odot) \text{ cm}^{-6}$ pc, implying our emission measure estimate is consistent with the observed value at the 1σ level. We also do not consider a separate temperature source in our calculation that could add another component to the observed emission measure, which would also explain the initial discrepancy.

The addition of the AGN ESO 141-G055 to our target list allows us to discuss our halo model in the context of recent observations by the *Fermi Gamma-ray Space Telescope*, which revealed two large gamma-ray emitting bubbles above and below the galactic plane (Su et al. 2010). These *Fermi* bubbles are aligned with features seen in the *ROSAT* soft X-ray maps and are believed to be interacting with the Galactic halo gas as they expand away from the Galactic plane. Although these *Fermi* bubbles are considerably hotter than the Galactic halo gas, they will still contribute free electrons to lines of sight toward the Galactic center. For this comparison, we can use the dispersion measure toward the Galactic center, which is sensitive to the total electron density along a given line of sight. Taylor & Cordes (1993) showed that the dispersion measure toward the Galactic center is 650 - 800 cm^{-3} pc, which is thought to be primarily due to free electrons from gas in the 10^3 - 10^4 K range (the warm ionized medium) (Gaensler et al. 2008). The contribution from our Galactic halo model toward the galactic center is only $\text{DM} = 72 \text{ cm}^{-3}$ pc, which is negligible compared to the model expectations. The contribution from these *Fermi* bubbles also appears to be negligible and even less than that of our Galactic halo model. Guo & Mathews (2012) and Yang et al. (2012) modeled the *Fermi* bubbles, assuming an ambient medium similar to our determined halo model, to recreate the bubbles' observed structure and found an average density in the plane of $\sim 10^{-3} \text{ cm}^{-3}$. This results in a dispersion measure toward the galactic center of $\text{DM} = 24 \text{ cm}^{-3}$ pc. Thus, both the *Fermi* bubbles and Galactic halo contribute a small fraction ($\sim 10\%$) of the total electrons near the Galactic plane.

The sightline toward ESO 141-G055 has a peculiarity in the ion column densities that are detected which is directly related to the presence of the *Fermi* bubbles. Most of our present sample shows little or no O VIII absorption, which allows us to constrain the temperature of the Galactic halo gas. However, the line of sight toward ESO 141-G055 suggests an enhancement of O VIII, with a column density ratio of $N(\text{O VIII})/N(\text{O VII}) = 1.4 \pm 0.5$. Yang et al. (2012) are able to produce the observed O VIII/O VII ratio and find that the shocked region of the bubbles is $\sim 10^8$ K while the interior is 10^7 - 10^8 K. This implies little contribution from O VII or O VIII to the total electron column along the line of sight. While the ion fractions of both ions are small inside the bubbles ($f \ll 0.1$), the O VIII ion fraction is at least an order of magnitude higher than the O VII fraction everywhere inside the bubbles. This results in the enhancement of O VIII relative to O VII for any line of sight that passes through the *Fermi* bubbles. However, these results do not explain the infrequent detection of O VIII along most of our other sightlines. A more detailed analysis of the density and temperature structure of the bubbles is beyond the scope of this work and will be the topic of a future project.

4.3. Thermal Considerations

The thermal properties of the hot gas halo (mainly the cooling time and radius) can be used as a measure of how large the halo could be if it were stable. We first adopt an expression for the cooling time (Fukugita & Peebles 2006):

$$\tau(r) = \frac{1.5nkT}{\Lambda(T, Z)n_e(n - n_e)} \approx \frac{1.5kT \times 1.92}{\Lambda(T, Z)n_e \times 0.92} \quad (10)$$

which assumes a primeval helium abundance. The cooling time as a function of radius can be seen in Figure 9 for different metallicities.

One result to note is that the cooling time is less than a Hubble time for a solar metallicity halo out to near the virial radius, implying a need for a continuous heating source if the halo were stable. This can be explained if the primary source of the halo gas is feedback from the disk in the form of supernovae or AGN, which would enrich and heat the halo. This allows the cooling time of the halo to be less than the Hubble time since the halo would receive an input of energy, making it stable throughout the Milky Way’s lifetime. Alternatively, if the halo gas is primarily accreted material by the Milky Way, the gas metallicity would be sub-solar. This implies a cooling radius between 30 - 40 kpc for a $\sim 0.3 Z_\odot$ halo, so the halo at $r > r_{cool}$ could not have cooled since the formation of the Milky Way.

We compare the cooling time as function of radius to the sound crossing time as a function of radius to determine if the Milky Way’s hot gas halo is in hydrostatic equilibrium. We assume that the halo is isothermal at a temperature of $\log T = 6.1$, which results in a sound speed of $c_s \sim 130 \text{ km s}^{-1}$. Figure 9 shows that the sound crossing time is smaller than the cooling for $r \gtrsim 1 \text{ kpc}$, implying the halo is in hydrostatic equilibrium.

The cooling time discussed above also has implications for the cooling and accretion rates of the Galactic halo gas on the disk of the Milky Way. The accretion rate is determined by integrating the mass within a radial shell divided by the cooling time at a given radius and can be seen in Figure 10. The sensitivity of the result on metallicity has various implications. For a solar metallicity halo, the accretion rate is similar to modeled accretion rates of similar mass spiral galaxies (Fraternali & Binney 2008). Figure 10 also indicates that the accretion rate is broadly consistent with the current observed star formation rate (SFR) in the Milky Way of 0.68 - 1.45 $M_\odot \text{ yr}^{-1}$ (Robitaille & Whitney 2010). This implies that the cooling of the Galactic halo may be a significant source of cold gas that fuels star formation in the disk of the Milky Way. However, there is also evidence indicating the observed Milky Way SFR can be balanced by stellar mass loss alone. Leitner & Kravtsov (2011) modeled mass loss rates for single-age stellar populations and determined star formation histories for several galaxies using the relationship between SFR and stellar mass in star-forming galaxies. Their results indicate that in most of their sample, including the Milky Way, mass loss from later stages of stellar evolution can more than compensate for the current observed SFRs. This indicates that the sub-solar metallicity accretion rate of 0.1 - 0.5 $M_\odot \text{ yr}^{-1}$ from the halo is more likely than a solar metallicity accretion rate if the mass supply rate is to be less than the observed SFR. If the halo has a solar metallicity ($\sim 1.0 M_\odot \text{ yr}^{-1}$) and stellar mass loss contributes $\sim 1.5 M_\odot \text{ yr}^{-1}$ back to the Milky Way disk, then the Milky Way’s SFR should increase with time. This opposes the observed cosmic SFR, indicating that the halo is likely not entirely at a solar metallicity (Borch et al. 2006). Another possibility that prevents the halo

cooling rate from overproducing the observed Milky Way SFR is a heating agent for the halo gas, such as supernovae. The addition of a heating source increases the cooling time of the halo gas, particularly near the stellar disk, and can significantly reduce the amount of gas cooling out of the halo.

The luminosity of the Galactic halo can be determined from the measured cooling rate discussed above. The conversion between the 0.5 - 2 keV luminosity and cooling rate is

$$L_X(r) = 0.362 \times \dot{M} \frac{1.5kT}{\mu m_p} \quad (11)$$

where \dot{M} is the cooling rate and 0.362 is the conversion between the bolometric luminosity and the 0.5 - 2 keV band luminosity. For typical cooling rates seen in Figure 10 and a solar gas metallicity, the corresponding 0.5 - 2 keV band luminosity is $\sim 7 \times 10^{39}$ erg s⁻¹. This is larger than what has been determined from *ROSAT* measurements of the diffuse X-ray background (Snowden et al. 1997), which imply $L_X \sim 2 \times 10^{39}$ erg s⁻¹. The difference is likely due to the uncertainty in the gas metallicity. A solar metallicity halo should be considered as an upper limit to \dot{M} since only part of the halo is expected to be enriched. In order to match the luminosity determined by *ROSAT*, the metallicity would need to be $\sim 0.3 Z_\odot$. Thus, our luminosity is broadly consistent with previous estimates of the Milky Way's diffuse X-ray luminosity if the average metallicity is less than solar.

If we assume that this hot halo is volume filling we can compare the pressure of this hot halo with other phases of the ISM. In particular, we compare our model pressure to pressures associated with HVCs measured by Fox et al. (2005), which are at temperatures ranging from $10^4 \sim 10^5$ K. In their analysis, they average six HVC models to find thermal pressures of $P/k = [530, 140, 50]$ cm⁻³ K at distances of [10, 50, 100] kpc. If we assume a temperature of $\log T = 6.1$, our model results in a range of pressures of $P/k = [694, 41, 24]$ cm⁻³ K for $r = [10, 50, 100]$ kpc respectively. This indicates that our hot gas is close to pressure equilibrium with these observed HVCs. However, it should be noted that the distances toward these HVCs are not well constrained and the results here are strongly dependent on both the density and temperature of the gas. We also do not consider the addition of a hotter gas phase in our analysis which would add an additional pressure component.

4.4. Final Comments

The goal of this study was to constrain the density profile of the Milky Way's hot gas halo better than previous studies, which have primarily relied upon simple models of the halo structure. We use *XMM-Newton* RGS archival data of 29 sightlines to analyze O VII absorption from the halo. One limitation of our analysis is the inability of the RGS to resolve the observed absorption lines. This prohibits us from analyzing the true saturation effects in the lines. From Table 2, accounting for line saturation with a Doppler width of 150 km s⁻¹ increases n_o of our density model but steepens the best-fit β compared to the optically thin fitting results. The parameter

n_o increases since all of the inferred column densities increase if we assume any line saturation. The parameter β also increases since the lines that have the largest equivalent widths, and thus the largest inferred column densities, also have large uncertainties in the curve of growth analysis. Table 4 shows the most important results of our analysis assuming both optically thin and saturated best-fit parameters from Table 2. By using saturated column densities, the steeper β parameter is more important than the increased normalization relative to the optically thin results in terms of the overall mass estimate. However, the inferred masses assuming the lower metallicity limits established by the pulsar dispersion measure toward the LMC result in comparable masses for each case. The emission measure estimates toward $l = 90^\circ$, $b = +60^\circ$ differ by a factor of ~ 2 , which is also due to the steeper β in the saturated parameter case. Neither of these estimates overproduce the observed emission measure for a solar metallicity, implying an additional component to the observed emission measure. By comparing our best-fit results for optically thin and saturated column densities, we find the best-fit parameters change, but the inferred masses from the best-fit profiles are similar.

The metallicity of the halo gas has not been thoroughly analyzed for the Milky Way’s halo and is crucial for understanding various properties of the halo gas. Although we initially assumed a solar metallicity halo in our analysis, we recognize that the metallicity of the gas is a large uncertainty in our analysis and is likely sub-solar. We are able to place a constraint on the metallicity of the gas between the Sun and the LMC based on the observed pulsar dispersion measure (Anderson & Bregman 2010). The metallicity of the gas must be $Z \gtrsim 0.2 Z_\odot$ to satisfy the pulsar dispersion measure constraint. This lower limit applies to the average metallicity of the gas between the Sun and the LMC ($r \approx 55$ kpc) and does not necessarily apply to halo gas beyond the LMC. Our results for the mass accretion rate and X-ray luminosity of the halo suggest that a halo metallicity of $Z = 0.3 Z_\odot$ is more appropriate. This metallicity is consistent with cosmological simulations (Toft et al. 2002; Cen & Ostriker 2006) and observations of both spiral galaxies (Rasmussen et al. 2009; Meiring et al. 2013) and some HVCs (Gibson et al. 2000; van Woerden & Wakker 2004; Fox et al. 2005). We also ignore a metallicity gradient in our analysis, which is possible from the mixing of ejected gas from the disk of the Milky Way and cooling primordial gas from the formation of the Milky Way. Both mechanisms are likely contributing to the halo gas, but the metallicity gradient of the halo gas is not well understood. An analysis of the halo gas metallicity and on the extent there exists a metallicity gradient will be critical in determining several halo gas properties.

With the density profile of the halo constrained, we are able to analyze useful properties of the halo and determine how the halo relates to the baryon content of the Milky Way. We find the mass contained in the halo for our best-fit parameters is between $M(18 \text{ kpc}) = 7.3^{+22.3}_{-4.3} \times 10^8 M_\odot$ and $M(200 \text{ kpc}) = 4.0^{+5.7}_{-0.7} \times 10^{10} M_\odot$ for an assumed metallicity $Z = 0.3 Z_\odot$. If we assume a lower estimate of the virial mass of the Milky Way ($1 \times 10^{12} M_\odot$) and the gas extending to the virial radius of the Milky Way for a halo that size, the largest baryon fraction we obtain is f_b (160 kpc) = $0.07^{+0.03}_{-0.01}$. This accounts for 10% - 50% of the missing baryons required to match the universal

baryon fraction of $f_b = 0.171$.

The constraints we place on the Milky Way’s hot gas halo are close to the best we are able to accomplish with *Chandra* and *XMM-Newton*. Improvements can be made on eliminating the degeneracy between the parameters n_o and r_c with additional Galactic targets near the Galactic center, however this does not affect the global properties of the halo. There is also work to be done exploring the interaction between the hot gas halo and the *Fermi* bubbles. The combination of O VII and O VIII emission will reveal the temperature structure just outside and inside the bubbles, which will help probe the contribution of thermal and non-thermal electrons inside the bubbles.

The authors would like to acknowledge valuable advice and conversations with Mike Anderson, Jimmy Irwin, Jon Miller, Mateusz Ruszkowski, Steve Snowden and Hsiang-Yi Yang. Financial support is gratefully acknowledged from NASA under the ADAP program.

REFERENCES

- Anderson, M. E., & Bregman, J. N. 2010, *ApJ*, 714, 320
- . 2011, *ApJ*, 737, 22
- Begelman, M. C., & Fabian, A. C. 1990, *MNRAS*, 244, 26P
- Binney, J., & Tremaine, S. 2008, *Galactic Dynamics: Second Edition*, ed. Binney, J. & Tremaine, S. (Princeton University Press)
- Blitz, L., & Robishaw, T. 2000, *ApJ*, 541, 675
- Borch, A., Meisenheimer, K., Bell, E. F., et al. 2006, *A&A*, 453, 869
- Bowen, D. V., Jenkins, E. B., Tripp, T. M., et al. 2008, *ApJS*, 176, 59
- Boylan-Kolchin, M., Bullock, J. S., Sohn, S. T., Besla, G., & van der Marel, R. P. 2013, *ApJ*, 768, 140
- Bregman, J. N., & Houck, J. C. 1997, *ApJ*, 485, 159
- Bregman, J. N., & Lloyd-Davies, E. J. 2007, *ApJ*, 669, 990
- Cen, R. 2012, *ApJ*, 753, 17
- Cen, R., & Ostriker, J. P. 2006, *ApJ*, 650, 560
- Costantini, E., Pinto, C., Kaastra, J. S., et al. 2012, *A&A*, 539, A32
- Dai, X., Anderson, M. E., Bregman, J. N., & Miller, J. M. 2012, *ApJ*, 755, 107

- Dunkley, J., Spergel, D. N., Komatsu, E., et al. 2009, *ApJ*, 701, 1804
- Fang, T., Mckee, C. F., Canizares, C. R., & Wolfire, M. 2006, *ApJ*, 644, 174
- Feldmann, R., Hooper, D., & Gnedin, N. Y. 2013, *ApJ*, 763, 21
- Fox, A. J., Savage, B. D., Wakker, B. P., et al. 2004, *ApJ*, 602, 738
- Fox, A. J., Wakker, B. P., Savage, B. D., et al. 2005, *ApJ*, 630, 332
- Fraternali, F., & Binney, J. J. 2008, *MNRAS*, 386, 935
- Fukugita, M., & Peebles, P. J. E. 2006, *ApJ*, 639, 590
- Gaensler, B. M., Madsen, G. J., Chatterjee, S., & Mao, S. A. 2008, *PASA*, 25, 184
- Gibson, B. K., Giroux, M. L., Penton, S. V., et al. 2000, *AJ*, 120, 1830
- Grcevich, J., & Putman, M. E. 2009, *ApJ*, 696, 385
- Guo, F., & Mathews, W. G. 2012, *ApJ*, 756, 181
- Gupta, A., Mathur, S., Krongold, Y., Nicastro, F., & Galeazzi, M. 2012, *ApJ*, 756, L8
- Hagihara, T., Yamasaki, N. Y., Mitsuda, K., et al. 2011, *PASJ*, 63, 889
- Hagihara, T., Yao, Y., Yamasaki, N. Y., et al. 2010, *PASJ*, 62, 723
- Holweger, H. 2001, in American Institute of Physics Conference Series, Vol. 598, Joint SOHO/ACE workshop "Solar and Galactic Composition", ed. R. F. Wimmer-Schweingruber, 23–30
- Kwak, K., & Shelton, R. L. 2010, *ApJ*, 719, 523
- Lehner, N., Howk, J. C., Thom, C., et al. 2012, *MNRAS*, 424, 2896
- Leitner, S. N., & Kravtsov, A. V. 2011, *ApJ*, 734, 48
- Li, J.-T., Li, Z., Wang, Q. D., Irwin, J. A., & Rossa, J. 2008, *MNRAS*, 390, 59
- McCammon, D., Almy, R., Apodaca, E., et al. 2002, *ApJ*, 576, 188
- Meiring, J. D., Tripp, T. M., Werk, J. K., et al. 2013, *ApJ*, 767, 49
- Nicastro, F., Zezas, A., Drake, J., et al. 2002, *ApJ*, 573, 157
- O’Sullivan, E., Ponman, T. J., & Collins, R. S. 2003, *MNRAS*, 340, 1375
- Paerels, F. B. S., & Kahn, S. M. 2003, *ARA&A*, 41, 291
- Rasmussen, A., Kahn, S. M., & Paerels, F. 2003, *The IGM/Galaxy Connection. The Distribution of Baryons at z=0*, 281, 109

- Rasmussen, J., Sommer-Larsen, J., Pedersen, K., et al. 2009, *ApJ*, 697, 79
- Robitaille, T. P., & Whitney, B. A. 2010, *ApJ*, 710, L11
- Savage, B. D., Sembach, K. R., & Lu, L. 1997, *AJ*, 113, 2158
- Sembach, K. R., Wakker, B. P., Savage, B. D., et al. 2003, *ApJS*, 146, 165
- Sivakoff, G. R., Sarazin, C. L., & Carlin, J. L. 2004, *ApJ*, 617, 262
- Snowden, S. L., Egger, R., Freyberg, M. J., et al. 1997, *ApJ*, 485, 125
- Strickland, D. K., Heckman, T. M., Colbert, E. J. M., Hoopes, C. G., & Weaver, K. A. 2004, *ApJS*, 151, 193
- Su, M., Slatyer, T. R., & Finkbeiner, D. P. 2010, *ApJ*, 724, 1044
- Sutherland, R. S., & Dopita, M. A. 1993, *ApJS*, 88, 253
- Taylor, J. H., & Cordes, J. M. 1993, *ApJ*, 411, 674
- Toft, S., Rasmussen, J., Sommer-Larsen, J., & Pedersen, K. 2002, *MNRAS*, 335, 799
- Tüllmann, R., Pietsch, W., Rossa, J., Breitschwerdt, D., & Dettmar, R.-J. 2006, *A&A*, 448, 43
- van Woerden, H., & Wakker, B. P. 2004, *High Velocity Clouds*, 312, 195
- Wakker, B. P., Savage, B. D., Sembach, K. R., et al. 2003, *ApJS*, 146, 1
- Wang, Q. D., Yao, Y., Tripp, T. M., et al. 2005, *ApJ*, 635, 386
- Williams, R. J., Mathur, S., Nicastro, F., et al. 2005, *ApJ*, 631, 856
- Yang, H.-Y. K., Ruszkowski, M., Ricker, P. M., Zweibel, E., & Lee, D. 2012, *ApJ*, 761, 185
- Yao, Y., & Wang, Q. D. 2005, *ApJ*, 624, 751
- . 2007, *ApJ*, 658, 1088

Table 1. Absorption-Line Measurements

Number	Name	l ($^{\circ}$)	b ($^{\circ}$)	EW (mÅ)	Error (mÅ)	$N_{OVI,thin}$ (10^{15} cm^{-2})	Error (10^{15} cm^{-2})	$N_{model,thin}$ (10^{15} cm^{-2})	$N_{OVI,saturated}$ (10^{15} cm^{-2})	Error (10^{15} cm^{-2})	$N_{model,saturated}$ (10^{15} cm^{-2})
1	Mrk 421	179.83	65.03	11.8	0.8	4.12	2.53	4.62	5.36	3.61	4.54
2	PKS 2155-304	17.73	-52.24	13.7	1.9	4.79	2.60	7.55	6.56	4.06	8.97
3	3C 273	289.95	64.36	24.6	3.3	8.60	2.77	5.67	18.06	9.28	5.98
4	MCG-6-30-15	313.29	27.68	32.6	6.8	11.36	3.45	7.73	42.35	27.19	9.28
5	LMC X-3	273.57	-32.08	21.0	5.0	7.34	3.07	3.91	13.00	7.37	4.39
6	1 H 1426+428	77.49	64.90	11.6	4.1	4.04	2.90	5.52	5.21	3.99	5.78
7	Ark 564	92.14	-25.34	12.3	4.6	4.29	2.98	5.25	5.63	4.23	5.38
8	NGC 4051	148.88	70.09	24.6	3.1	8.59	2.74	4.80	18.02	9.18	4.77
9	NGC 3783	287.46	22.95	24.1	7.5	8.40	3.64	6.05	17.17	10.64	6.56
10	NGC 5548	31.96	70.50	7.0	6.8	2.43	3.45	6.07	2.79	6.06	6.59
11	Ark 120	201.69	-21.13	-6.0	5.5	-2.08	3.16	4.16	-2.34	5.11	3.94
12	PKS 0558-504	257.96	-28.57	21.7	7.8	7.58	3.70	4.97	13.83	8.86	5.00
13	Mrk 766	190.68	82.27	0.1	6.8	0.05	3.45	5.06	0.07	4.27	5.12
14	NGC 4593	297.48	57.40	23.4	8.5	8.16	3.88	5.96	16.10	10.46	6.42
15	3C 390.3	111.44	27.07	27.4	7.3	9.56	3.57	4.75	23.65	14.46	4.71
16	NGC 7469	83.10	-45.47	1.6	8.9	0.57	4.01	5.51	0.59	5.57	5.75
17	Mrk 509	35.97	-29.86	25.9	7.3	9.04	3.57	8.62	20.36	12.39	10.89
18	3C 120	190.37	-27.40	13.8	9.2	4.81	4.09	4.15	6.59	5.83	3.94
19	NGC 3516	133.24	42.40	22.0	13.4	7.66	5.30	4.52	14.12	11.38	4.40
20	Ton 1388	223.36	68.21	34.5	15.7	12.04	6.03	4.83	54.68	45.38	4.82
21	1H 0414+009	191.82	-33.16	-3.1	14.8	-1.07	5.73	4.20	-1.14	10.16	4.00
22	MR 2251-178	46.20	-61.33	39.8	19.6	13.90	7.28	6.25	119.63	108.60	6.86
23	IC 4329a	317.50	30.92	33.8	19.3	11.78	7.20	7.93	49.41	43.14	9.65
24	Fairall 9	295.07	-57.83	31.1	16.4	10.84	6.27	5.89	35.30	29.08	6.31
25	MS 0737.9+7441	140.27	29.57	-13.8	20.7	-4.83	7.65	4.34	-6.65	6.57	4.18
26	3C 59	142.04	-30.54	60.9	19.2	21.24	7.15	4.33	2599.11	2463.75	4.16
27	ESO 141-G055	338.18	-26.71	21.4	5.3	7.48	3.12	10.75	13.48	7.69	15.06
28	4U 1820-30	2.79	-7.91	23.9	3.6	8.36	2.81	7.98	16.94	8.79	18.54
29	X1735-444	346.05	-6.99	24.7	9.7	8.61	4.23	5.02	18.15	12.32	9.98

Note. — Our sample consists of 26 AGN, two Galactic sources and one LMC source. The targets are listed in order of decreasing S/N with the exception of 27-29. These three targets are additions to the sample used by Bregman & Lloyd-Davies (2007). ESO 141-G055 is an AGN while 4U 1820-30 (located in the globular cluster NGC 6624) and X1735-444 are Galactic X-ray sources. All targets are used in our model fitting and analysis. The *thin* and *saturated* subscripts refer to column density conversions assuming the lines are optically thin or saturated assuming a constant Doppler width of 150 km s^{-1} . The *model* subscripts refer to the column densities along each line of sight resulting from the best-fit parameters found in Table 2.

Table 2. Model Fitting Results

Model	n_o (cm^{-3})	$r_c / R_c, z_c$ (kpc)	β	$n_o r_c^{3\beta}$ ($\text{cm}^{-3} \text{ kpc}^{3\beta}$)	χ^2 (dof)
Spherical - optically thin ^a	$0.09^{+0.14}_{-0.06}$	$0.33^{+0.25}_{-0.23}$	$0.56^{+0.10}_{-0.12}$	$0.013^{+0.016}_{-0.010}$	31.0 (26)
Spherical - saturated ^b	$0.46^{+0.74}_{-0.35}$	$0.35^{+0.29}_{-0.27}$	$0.71^{+0.13}_{-0.14}$	$0.049^{+0.341}_{-0.047}$	26.0 (26)
Approximated ^c	–	–	$0.71^{+0.17}_{-0.20}$	$0.048^{+0.085}_{-0.037}$	26.0 (27)
Flattened ^d	$0.46^{+0.74}_{-0.35}$	$0.42^{+0.16}_{-0.10}, 0.26^{+0.13}_{-0.09}$	$0.71^{+0.13}_{-0.14}$	–	29.4 (25)
Truncated sample ^e	$0.48^{+0.71}_{-0.43}$	$0.33^{+0.25}_{-0.23}$	$0.70^{+0.14}_{-0.14}$	$0.046^{+0.255}_{-0.045}$	26.0 (26)
S/N cut sample ^f	$0.51^{+0.72}_{-0.46}$	$0.20^{+0.18}_{-0.17}$	$0.60^{+0.12}_{-0.13}$	$0.028^{+0.124}_{-0.027}$	20.0 (20)

^aResults assuming the absorption lines are optically thin and a spherical density profile described by Equation (5).

^bResults assuming the absorption lines are saturated with a Doppler width of 150 km s^{-1} and a spherical density profile described by Equation (5).

^cResults assuming an approximated spherical density profile described by Equation (6).

^dResults assuming a flattened density profile described by Equation (7).

^eSame model as the spherical - saturated case, but with negative equivalent width measurements truncated at 0.

^fSame model as the spherical - saturated case, but while only analyzing observations in our sample with S/N greater than 1.1.

Table 3. Scale Heights

	R (kpc)					
	0	1	5	8.5	20	
	1	0.5	1.0	12.2	34.4	187.8
	2	1.0	1.2	6.8	17.9	94.6
z (kpc)	3	1.4	1.6	5.3	12.7	63.8
	4	1.9	2.0	4.8	10.3	48.7
	5	2.3	2.4	4.7	9.1	39.8

Table 4. Saturation Effects

	Optically Thin	Saturated
Added uncertainty to EW (mÅ)	7.5	7.2
$M(18 \text{ kpc}) (M_{\odot})$	$3.1^{+6.8}_{-1.9} \times 10^8$	$2.2^{+6.7}_{-1.3} \times 10^8$
$M(200 \text{ kpc}) (M_{\odot})$	$2.4^{+4.9}_{-0.5} \times 10^{10}$	$1.2^{+1.7}_{-0.2} \times 10^{10}$
$Z_{LMC} (Z_{\odot})$ ^a	0.4	0.2
$EM_{GalacticPole}(Z/Z_{\odot}) \text{ cm}^{-6} \text{ pc}$ ^b	0.0038	0.0018

^aLower limit placed on the gas metallicity based on the pulsar dispersion measure toward the LMC.

^bModel emission measures toward $l = 90^{\circ}$, $b = +60^{\circ}$.

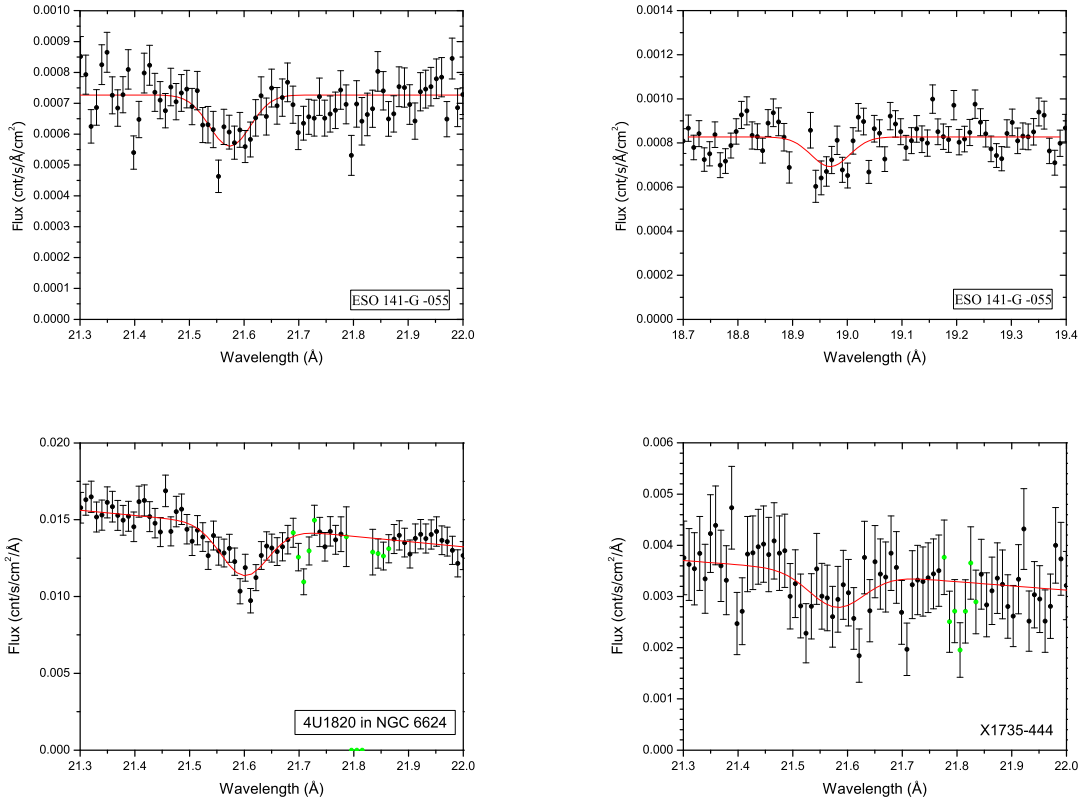


Fig. 1.— *XMM-Newton* flux of our additional targets at 21.60 Å (and 18.97 Å for ESO 141-G055) to show O VII and O VIII absorption. The continuum and line fitting procedure is the same used by Bregman & Lloyd-Davies (2007). There are instrumental features in the RGS near 21.82 Å and 18.91 Å (green points) that are not included in the continuum fitting procedure.

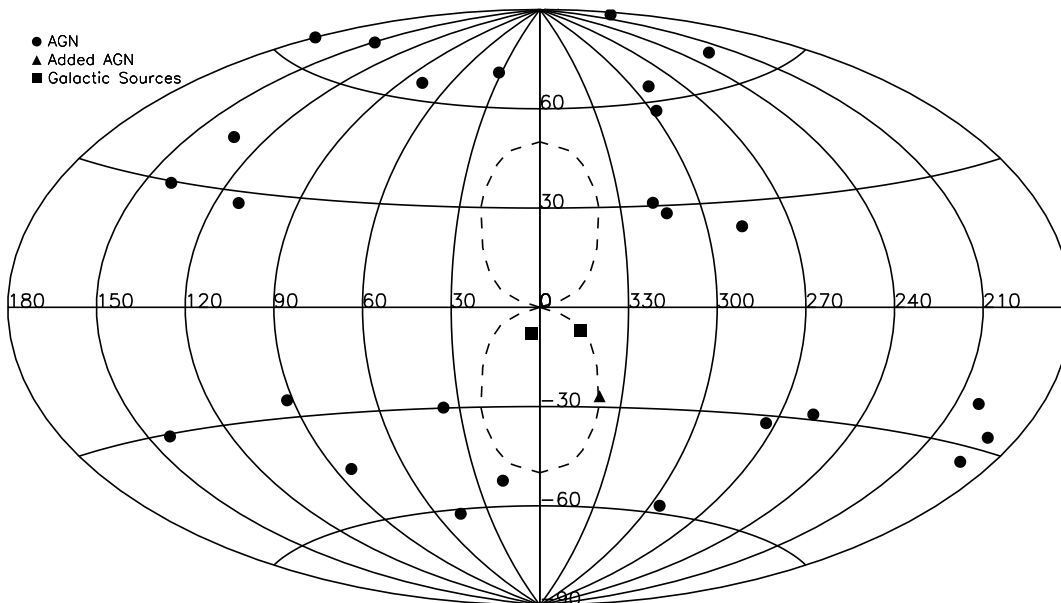


Fig. 2.— Distribution of our X-ray absorbing lines of sight on the sky. The sample from Bregman & Lloyd-Davies (2007) can be seen with solid circles while our additional targets can be seen as squares (Galactic sources) and a triangle (AGN). The dashed line represents the approximate edges of the north and south *Fermi* bubbles. The lines of sight of the three added targets pass through the south bubble and allow us to analyze the bubbles’ density and temperature structure.

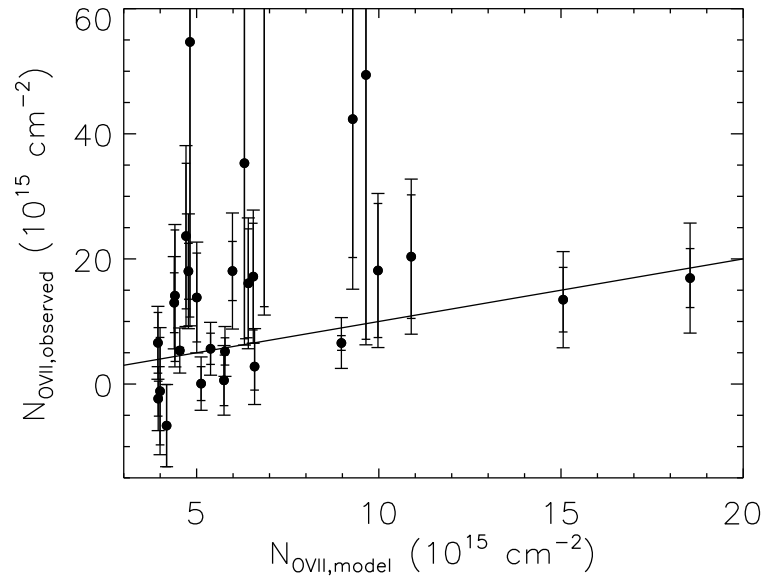


Fig. 3.— Comparison between our observed O VII column densities and best-fit model column densities in the saturated line case. The solid line indicates where the observed column density equals the model column density. The larger errors with larger tick marks for each point represent the initial error with the additional $7.2 \text{ m}\text{\AA}$ added to each target in order to obtain an acceptable χ^2 . For clarity, the targets MR 2251-178 and 3C 59 are not visible on the plot due to their large observed equivalent widths. However these lines of sight also have very large uncertainties and are both within 2σ of their model column densities.

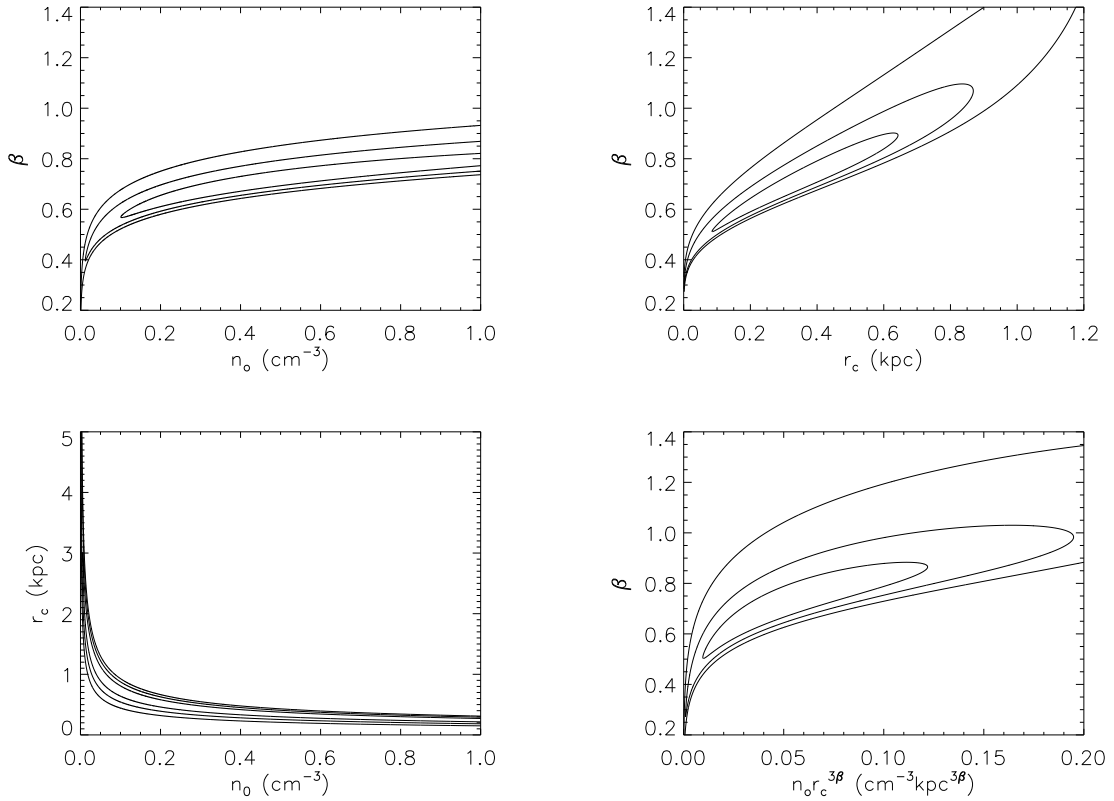


Fig. 4.— 1σ , 2σ , and 3σ contours for r_c , n_o , β , and $n_o r_c^{3\beta}$ for our spherical model and using saturated column densities assuming $b = 150 \text{ km s}^{-1}$. The elongation of the contours in the $r_c - n_o$ plane illustrates the degeneracy discussed in Section 3.2. The contours constraining $n_o r_c^{3\beta}$ are based on the parameters in Equation (2).

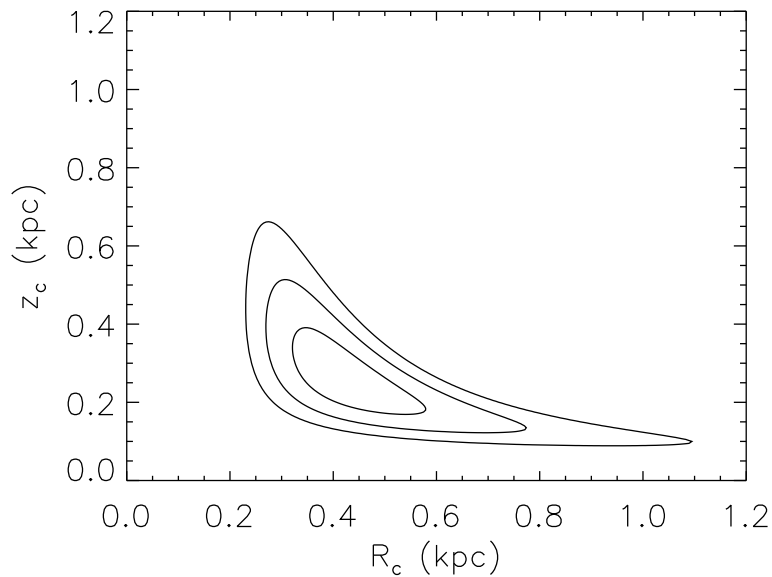


Fig. 5.— 1σ , 2σ , and 3σ contours for R_c and z_c for our flattened model. R_c corresponds to the core radius in the disk of the Milky Way and z_c corresponds to the core radius out of the plane of the Milky Way. The shape of the contours indicates that the halo is preferentially aligned with the disk of the Milky Way.

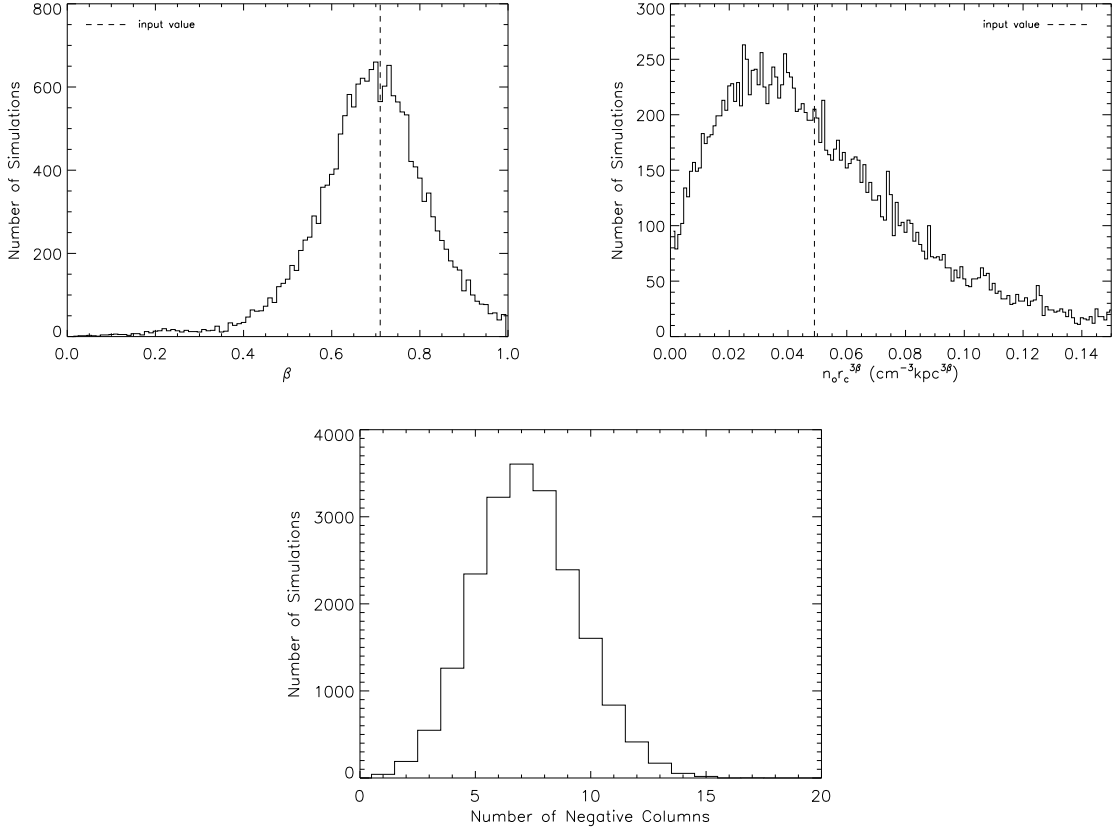


Fig. 6.— Histograms of best-fit parameters β and $n_0 r_c^{3\beta}$ in addition to the number of negative column densities for 20,000 Monte Carlo simulations. Our input values for each parameter were our best-fit parameters from Table 2. We found median values of 0.71 for β and $0.050 \text{ cm}^{-3} \text{ kpc}^{3\beta}$ for $n_0 r_c^{3\beta}$, which are consistent with the measured values of 0.71 and $0.048 \text{ cm}^{-3} \text{ kpc}^{3\beta}$ (dashed lines). The distributions and medians for β , $n_0 r_c^{3\beta}$, and other model parameters are consistent with our measured best-fit parameters and their 1σ uncertainties, implying we recover our best-fit model with negative column densities in our sample.

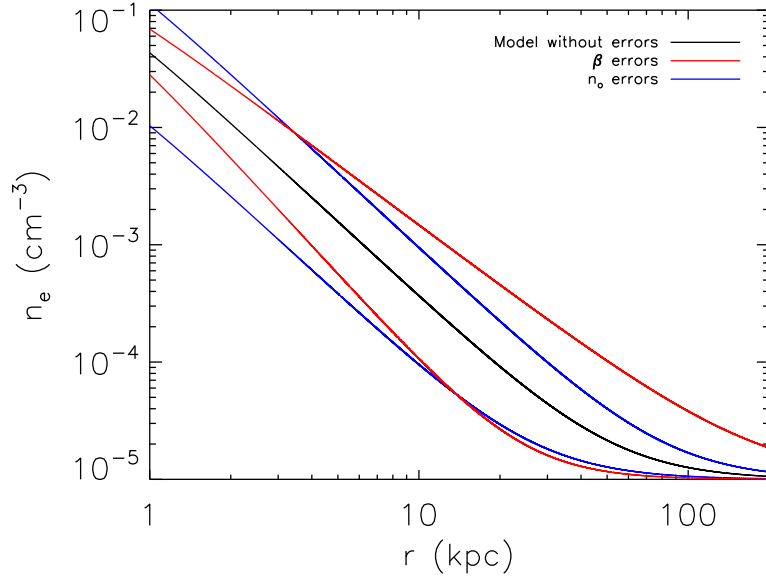


Fig. 7.— Density profile given our best-fit parameters (black line) with 1σ errors on β (red line) and n_o (blue line). The profile also includes an additional ambient medium of $n_e = 1 \times 10^{-5} \text{ cm}^{-3}$ to account for observed ram-pressure stripping of dwarf spheroidal galaxies.

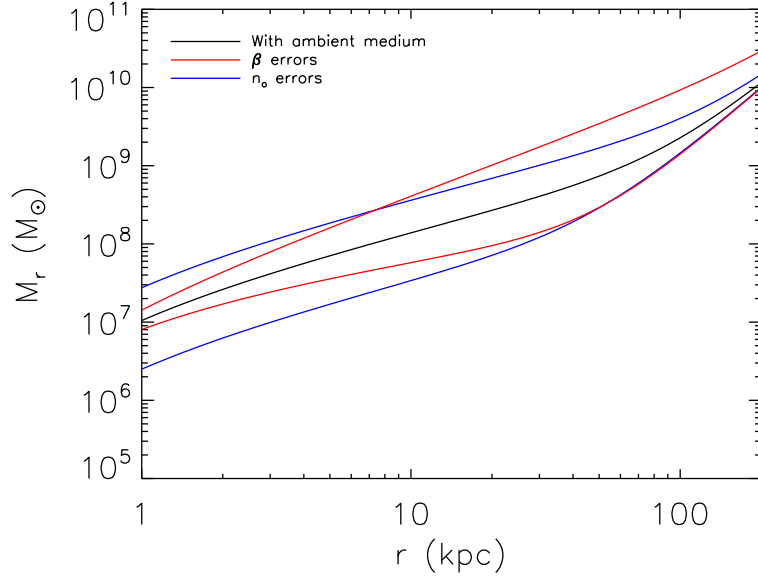


Fig. 8.— Enclosed mass as a function of radius with the same uncertainties as Figure 7. The enclosed mass of the halo is much smaller than the virial mass of the Milky Way and is only comparable to the stellar + cold gas mass of the Milky Way if the size is comparable to the virial radius of the Milky Way. The mass profile here is for solar metallicity gas.

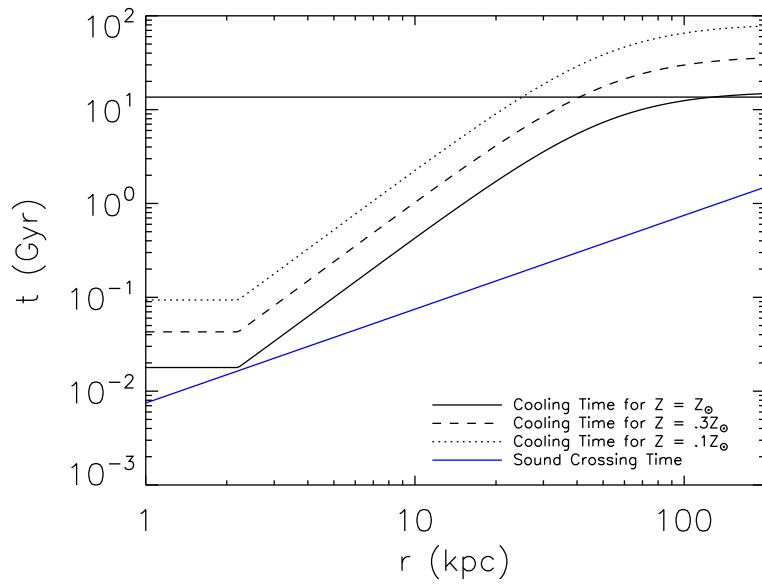


Fig. 9.— Cooling time as a function of radius given our best-fit parameters and assuming the halo is isothermal at $\log T = 6.1$. The cooling time is sensitive to the assumed metallicity of the halo and is comparable to a Hubble time at the Milky Way’s virial radius for solar metallicity gas. This implies that the halo either has a sub-solar metallicity or is subject to a continuous heating source. We also plot the sound crossing time as a function of galactocentric radius. This shows that the cooling time is greater than the sound crossing time at all radii, implying the halo is in hydrostatic equilibrium.

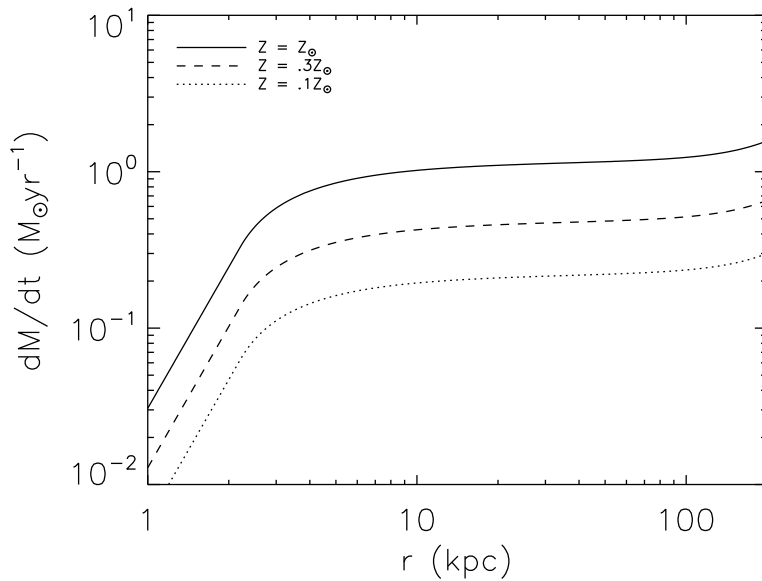


Fig. 10.— Cooling rate (or accretion rate) as a function of radius for our best-fit parameters. The solar metallicity gas results in an accretion rate that is roughly consistent with the SFR observed in the Milky Way, but sub-solar metallicity gas is more consistent with what has been observed in other spiral galaxies.